Periodic orbits in the doubly synchronous binary asteroid systems and their applications in space missions

Haibin Shang · Xiaoyu Wu · Pingyuan Cui

Abstract This paper investigates the periodic motion of a particle in the doubly synchronous binary asteroid systems. Two typical doubly synchronous systems, 809 Lundia and 3169 Ostro, are discussed in detail. Under the Roche figure assumption, the two bodies of doubly synchronous system can be modeled as two triaxial ellipsoids. The Ivory's theorem is used to derive the gravitational potential of the system. Then, a global numerical method, which combines grid searching and differential correction, is developed for systematically searching periodic orbits in the doubly synchronous systems. A total of 30 and 28 families of periodic orbits around Lundia and Ostro are found, respectively. Furthermore, on the basis of the analysis of morphology, stabilities and invariant manifolds, the potential applications of these periodic orbit families are studied. Several quasi-circular orbit families with low instability index are found to be suitable for the observation of the two typical binary systems. The invariant manifolds of some periodic orbits near the equilibrium points can provide the fuel-free trajectories to achieve the ballistic landing to the surface of the asteroids and transfer between the binary asteroids.

Keywords Binary asteroids · Doubly synchronous system · Periodic orbits · Invariant manifold

H. Shang (✉) · X. Wu · P. Cui
Beijing Institute of Technology, Beijing, China
e-mail: shanghb@bit.edu.cn

X. Wu
e-mail: wuxiaoyubit@yahoo.com

P. Cui
e-mail: cuipy@bit.edu.cn

1 Introduction

Nowadays exploring binary asteroids has gradually attracted many scientists and engineers since the first binary asteroid Ida–Dactyl was discovered by the Galileo spacecraft in 1993 (Helfenstein et al. 1996). Especially, one of the binary asteroids 1996 FG3 was selected as the backup target of the MarcoPolo-R mission led by the European Space Agency in recent years (Tardivel et al. 2013). The motivations of these missions are abundant, mainly including the fact that the origin of the binary asteroids may reveal the evolution of the solar system and the formation of solar planets. The research shows the binary asteroid systems have a delicate balance between disruption and cohesion forces (Tardivel and Scheeres 2013). Sending a spacecraft to the system can reveal the scientific results on the formation and future evolution of these bodies. Further, one of the benefits to go to a binary is that information can be obtained about two asteroids for essentially the price of one. Thus there is a way to access this information without affecting the mission cost and risks (Tardivel et al. 2013).

Binary systems compose the considerable fraction about 15 ± 4 % of the near-Earth asteroid population (Margot et al. 2002; Pravec et al. 2006), and about 2 % of the main belt population (Merline et al. 2002). Other binaries are from Mars crossing (Walsh et al. 2008), Trojan objects (Merline et al. 2002), and even Kuiper-belt objects (Noll et al. 2006). These binary systems can be simply sorted into three classifications based on their morphologies and spin rates of both components-asynchronous systems, synchronous systems, and doubly synchronous systems. Synchronous and doubly synchronous binaries are the most likely targets for human exploration missions, because they have stable states, characterized morphologies, and interesting dynamics. Different from the Circular Restricted Three Body Problem (CRTBP),

binary systems cannot simply be regarded as two mass particles due the close distance of two bodies. We must consider the mass distribution and shapes of both bodies. Bellerose and Scheeres (2008a) have used the ellipsoid-sphere model to discuss the motion in synchronous binary system 1999 KW4. Because these synchronous binaries have elongated secondary and nearly spherical primary with an equatorial bulge (Pravec et al. 2006; Pravec and Harris 2007), the assumed model is appropriate. However, more and more doubly synchronous binary asteroids (DSBAs) have been discovered in the last decade. Observations have found that most of DSBAs satisfy the Roche figure, which is an equilibrium figure of a rigidly spinning self-gravitating homogeneous fluid body (Descamps 2008). The Roche figures are similar to the double ellipsoid shapes with their minimum inertia axes aligned. Hence the two bodies of the DSBAs can be modeled as two triaxial ellipsoids suitably.

The periodic motion around DSBAs is deserved to be paid attention because it can relate to the dynamical mechanism of the systems, such as the further evolution of the systems and the formation of the natural satellites. Periodic orbits around the single asteroids have been researched in decades abundantly. Some special families of periodic orbits around the asteroid 4769 Castalia were computed using a detailed gravitational model of a polyhedron (Scheeres et al. 1996). A number of periodic orbits were also found in the time-periodic system, such as the asteroid 4179 Toutatis (Scheeres et al. 1998). Yu and Baoyin (2012a) discussed the periodic orbits in the vicinity of equilibrium points around the asteroid 216 Kleopatra. Recently, a total of 29 families of global periodic orbits around this asteroid were found by a hierarchical grid searching method (Yu and Baoyin 2012b).

Furthermore, the periodic orbits and their invariant manifolds can play a crucial role for the space mission design. Dichmann et al. (2003) discussed the applications of the Lyapunov, vertical, axial and 'backflip' orbits in the Earth-Moon system; Lo and Parker (2004) classified the simple planar periodic orbits in the CRTBP and applied their invariant manifolds for the transfer mission design. Making use of the planar Lyapunov orbits and their invariant manifolds, a possible maneuver to orbit the asteroid to observe it and later achieve vertical landing was proposed by Herrera-Sucarrat et al. (2014).

In this paper, the periodic motion in two typical DSBAs, 809 Lundia and 3169 Ostro, are discussed. The two bodies of the DSBA are modeled as two triaxial ellipsoids and their gravitational potential is derived in Sect. 2. In Sect. 3, we contribute to the investigation of the global periodic orbits in the DSBAs by applying a numerical method combing the initial grid searching and differential corrections. 30 families of periodic orbits around Lundia and 28 families around Ostro are found. Their morphology and stabilities are discussed. Further, the invariant manifolds of these periodic orbits are also computed. Section 4 deals with the potential

applications of these periodic orbits including space observation, ballistic landing and ballistic transfer.

2 Double ellipsoids model and equilibrium points

2.1 Roche figures of DSBAs

Doubly synchronous binary asteroids mainly include two groups, as showed in Table 1. The two groups are distinguished by the shapes of lightcurve (Descamps 2008). The first group consists of strictly speaking doubly synchronous asteroids with nearly similar-sized components preserving the same face towards each other all the time (Descamps et al. 2008), such as 90 Antiope (Descamps et al. 2007a), 854 Frostia (Behrend et al. 2006) and 809 Lundia (Kryszczyńska et al. 2009). The second group is composed of so called doubly synchronous contact-binaries considered as a special kind of double binaries with components so near to one another that they overlap to form a single body (Descamps et al. 2008), such as 3169 Ostro (Descamps et al. 2007b). Some orbital and physical properties for the selected DSBAs are also given in Table 1.

The basic characteristics of both groups of DSBAs can be described by the Roche figures: Assume that these binaries are formed by the fission of a "rubble pile" asteroid which is considered as a porous collection of gravitationally bound chunks. Consequently the shapes of these binaries obey the general results of rotating fluid mass theories (Descamps 2008). In 1849, a significant phenomenon that the equilibrium figures of homogeneous hydrostatic bodies moving synchronously around each other in circular orbit is found by Eduardo Roche. Consequently, these hydrostatic bodies are deformed into so called Roche ellipsoids (see Chandrasekhar 1969 for an extensive review). In addition, the shapes of these binaries subordinated to the general results of rotating fluid mass theories (Descamps 2008). Therefore, the DSBAs can be regarded as Roche systems. Recently, the Roche ellipsoid model is used to approximate the shapes and physical properties of some doubly synchronous asteroids by many researchers (Descamps 2008; Descamps et al. 2007a, 2007b; Kryszczyńska et al. 2009).

In this paper, two typical doubly synchronous systems, the double binary 809 Lundia, and the contact binary 3169 Ostro are discussed in detail. Their Roche ellipsoid solutions are listed in Table 2 and the spatial views of their Roche shapes are shown in Fig. 1.

2.2 Equations of motion

In this section, the equations of motion of a particle in the rotating coordinate are established first. The mass of both

Table 1 Orbital and physical properties for the selected doubly synchronous binary systems

Notes. The data above refer to the references Descamps et al. 2008; Pravec and Harris 2007, and to the database available on web page http://www.asu.cas.cz/~asteroid/binastdata.htm. a is the semi-major axis, ρ is the bulk density, D_p and D_s are the mean diameters at the equatorial of the primary and the secondary, P_{orb} is the orbital period, P_p and P_s are primary and secondary rotation periods. Values in the parentheses are estimated or derived using less reliable data or with some unusual assumptions

Asteroid	a (km)	ρ (g/cm^3)	D_p (km)	D_s (km)	P_{orb} (h)	P_p (h)	P_s (h)
Doubly synchronous asteroids							
90 Antiope	171	1.19	86.7	82.8	16.5051	16.5051	16.5051
617Patroclus	680	1.3	101	93	102.8	(102.8)	(102.8)
809 Lundia	(15)	1.64	6.9	6.1	15.418	15.418	15.418
854 Frostia	(24)	0.9	5.7	6	37.711	(37.711)	(37.711)
1089 Tama	(21)	2.5	9.1	8	16.4461	(16.4461)	(16.4461)
1139 Atami	(15)	(2.0)	5	4.0	27.45	(27.45)	(27.45)
1313 Berna	(30)	1.2	9.5	9.2	25.464	(25.464)	(25.464)
2478 Tokai	(23)	(2.0)	7.6	6.6	25.897	25.897	25.897
4492 Debussy	(40)	0.9	12.6	12	26.606	(26.606)	(26.606)
4951 Iwamoto	(35)	(2.0)	4.2	3.7	118.0	118.0	118.0
7369 Gavrilin	(20)	(2.0)	4.6	3.2	49.12	(49.12)	(49.12)
Doubly synchronous contact-binaries							
624 Hektor	1178	2.2	(225.0)	15.0	6.921	6.921	6.921
3169 Ostro	4.8	2.6	3.6	3.1	6.509	6.509	6.509
69230 Hermes	(1.2)	1.9	0.6	0.54	13.894	(13.894)	(13.894)

Table 2 Roche ellipsoid models of 3169 Ostro and 809 Lundia

Parameter	Lundia	Ostro
Separation	15.8 km	4.8 km
Mass ratio	0.5917	0.6151
Density	1.64 g/cm^3	2.6 g/cm^3
Primary		
Largest axis (a_1)	3.9 km	2.4 km
Intermediate axis (b_1)	3.3 km	1.3 km
Shortest axis (c_1)	3.2 km	1.2 km
Secondary		
Largest axis (a_2)	3.5 km	2.2 km
Intermediate axis (b_2)	2.9 km	1.7 km
Shortest axis (c_2)	2.8 km	1.6 km

Fig. 1 Spatial views of the Roche models of Lundia and Ostro

ellipsoids can be represented by M_1 and M_2 respectively. The mass ratio of the system is defined as

$$\mu = \frac{M_1}{M_1 + M_2} \tag{1}$$

The semi-major axes of both ellipsoids are a_1, b_1, c_1 and a_2, b_2, c_2, respectively. Note that $0 \leq c_1 \leq b_1 \leq a_1$ and $0 \leq c_2 \leq b_2 \leq a_2$. R represents the distance between two bodies. While $\boldsymbol{R}_1$ and $\boldsymbol{R}_2$ represent the position vectors from the origin of the coordinate to the center of two bodies. And the norm of $\boldsymbol{R}_1$ and $\boldsymbol{R}_2$ are

$$R_1 = |\boldsymbol{R}_1| = (1 - \mu)R \tag{2}$$

$$R_2 = |\boldsymbol{R}_2| = \mu R \tag{3}$$

We now consider a particle moving in the gravitational field of the binary systems, where $\boldsymbol{l}$ stands for the position vector of particle relative to origin, as shown in Fig. 2.
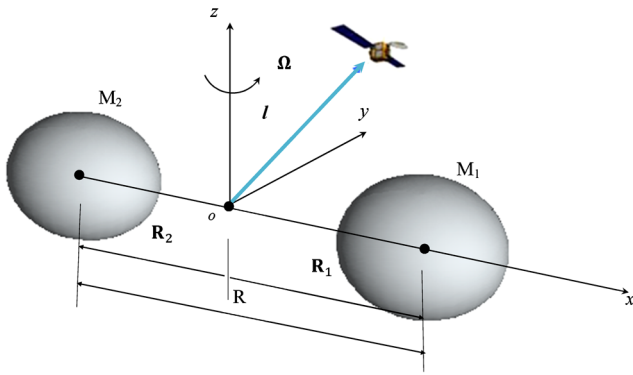
Fig. 2 The double ellipsoids model of doubly synchronous binary systems

Scheeres and Augenstein (2004) presented the vector form of the equation of motion in the rotating frame fixed to the mass center of the system as

$$\ddot{l} + 2\boldsymbol{\Omega} \times \dot{l} + \boldsymbol{\Omega} \times (\boldsymbol{\Omega} \times l) = G(M_1 + M_2) \frac{\partial \hat{U}_{sys}}{\partial l} \quad (4)$$

where G is the gravitational constant, $\hat{U}_{sys}$ is the system's gravitational potential. $\boldsymbol{\Omega}$ is the synchronous angular velocity. (Assume that the system rotates uniformly with $\dot{\boldsymbol{\Omega}} = 0$.)

On the other hand, because of synchronicity and conservation, the binary system is an autonomous system, and the gravitational potential satisfies Laplace's equation. Therefore, the system's exterior potential can be superposed from both ellipsoids. For a single uniform density ellipsoid with size a, b, c, the exterior potential is derived in Ivory's Theorem, expressed as

$$\hat{U}(r) = \frac{3}{4} GM \int_{\lambda(r)}^{\infty} \phi(r, \upsilon) \frac{d\upsilon}{\Delta(\upsilon)} \quad (5)$$

$$\phi(r, \upsilon) = 1 - \frac{x^2}{a^2 + \upsilon} - \frac{y^2}{b^2 + \upsilon} - \frac{z^2}{c^2 + \upsilon} \quad (6)$$

$$\Delta(\upsilon) = \sqrt{(a^2 + \upsilon)(b^2 + \upsilon)(c^2 + \upsilon)} \quad (7)$$

where $r = x\boldsymbol{i} + y\boldsymbol{j} + z\boldsymbol{k}$, $\lambda(r)$ satisfies $\phi(r, \upsilon) = 0$. According to potential superposition, we can define the system's gravitational potential

$$\hat{U}_{sys} = \hat{U}_1(l - R_1) + \hat{U}_2(l - R_2) \quad (8)$$

In order to simplify the analysis, we introduce the normalizations. Take the maximum semi-major axis a_1 of the primary as the length scale, and the mean motion $n = \sqrt{G(M_1 + M_2)/a_1^3}$ as the frequency scale. Thus the normalized positions and angular velocity are

$$\rho = \frac{R}{a_1}, \qquad r_1 = \frac{R_1}{a_1}, \qquad r_2 = \frac{R_2}{a_1}, \qquad r = \frac{l}{a_1} \quad (9)$$

$$\boldsymbol{\omega} = \frac{\boldsymbol{\Omega}}{n} \quad (10)$$

The normalized form of Eqs. (4) and (8) are

$$\ddot{r} + 2\boldsymbol{\omega} \times \dot{r} + \boldsymbol{\omega} \times (\boldsymbol{\omega} \times r) = \frac{\partial U_{sys}}{\partial r} \quad (11)$$

$$U_{sys} = U_1 + U_2 = \mu U(r - r_1) + (1 - \mu) U(r - r_2) \quad (12)$$

with

$$U(r) = \frac{3}{4} \int_{\lambda(r)}^{\infty} \phi(r, \upsilon) \frac{d\upsilon}{\Delta(\upsilon)} \quad (13)$$

The equations of motion Eqs. (11) and (12) can be restated in an (x, y, z) coordinate system, i.e.

$$\begin{cases} \ddot{x} - 2\omega\dot{y} - \omega^2 x = -\mu(x - r_1)E_{a1} - (1 - \mu)(x + r_2)E_{a2} \\ \ddot{y} + 2\omega\dot{x} - \omega^2 y = -\mu y E_{b1} - (1 - \mu)y E_{b2} \\ \ddot{z} = -\mu z E_{c1} - (1 - \mu)z E_{c2} \end{cases}$$

$$(14)$$

The E_a, E_b, E_c expressions are the elliptic integrals, which represent the mass distribution of both ellipsoids. The computing methods of elliptic integrals are presented in Neutsch (1979).

2.3 Zero velocity curves

Due to the explicit time independence of the Hamiltonian function, an integral of generalized energy exists, which can be expressed as

$$H = \frac{1}{2}\dot{r} \cdot \dot{r} - \frac{1}{2}(\boldsymbol{\omega} \times r) \cdot (\boldsymbol{\omega} \times r) - U_{sys} \quad (15)$$

Because H is time-invariant, it also allows for an important integral constant, the Jacobi constant C, which describes total energy of a particle relative to the rotating frame, i.e.,

$$C = \frac{1}{2}(\dot{x}^2 + \dot{y}^2 + \dot{z}^2) - \frac{1}{2}\omega^2(x^2 + y^2)$$
$$- \mu U(r - r_1) - (1 - \mu)U(r - r_2) \quad (16)$$

where, $(\dot{x}^2 + \dot{y}^2 + \dot{z}^2)/2$ is the kinetic energy relative to the rotating frame; $-\omega^2(x^2 + y^2)/2$ represents the potential energy of the centrifugal force induced by the rotation of the reference frame; $-\mu U(r - r_1)$ and $-(1 - \mu)U(r - r_2)$ are the gravitational potential energies of the two ellipsoidal bodies.

The solution of $(\dot{x}^2 + \dot{y}^2 + \dot{z}^2)/2 = 0$ represents the velocity of a particle reaching zero in the rotating frame coordinate. In other words, the particle would collide with and rebound off of the boundaries which are known as the zero-velocity curves. Figure 3 demonstrates the zero-velocity
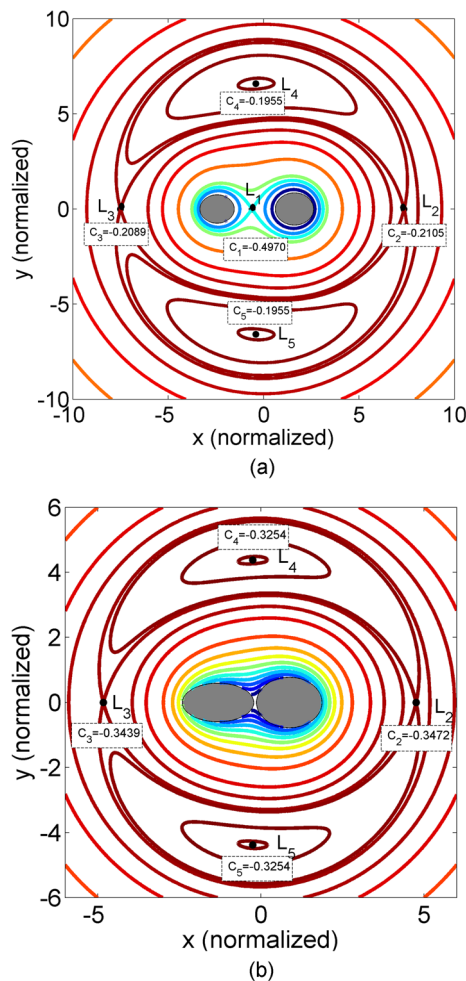
Table 3 Equilibrium points of Lundia system

Equilibrium point	(x, y, z)	Jacobi constant
L_1	$(-0.5484, 0, 0)$	-0.4970
L_2	$(7.9354, 0, 0)$	-0.2105
L_3	$(-8.0461, 0, 0)$	-0.2089
L_4	$(-0.3436, 7.2077, 0)$	-0.1955
L_5	$(-0.3436, -7.2077, 0)$	-0.1955

Table 4 Equilibrium points of Ostro system

Equilibrium point	(x, y, z)	Jacobi constant
L_1	–	–
L_2	$(4.7494, 0, 0)$	-0.3472
L_3	$(-4.8030, 0, 0)$	-0.3439
L_4	$(-0.2782, 4.3758, 0)$	-0.3254
L_5	$(-0.2782, -4.3758, 0)$	-0.3254

vided into two parts: A particle will never approach the bodies in the outer branch while the particle in the inner branch will keep orbiting or end up colliding with the asteroids.

When $C_2 < C < C_3$ in both systems, the two allowable regions merge into one. The particle can move from the inner region into the outer one through the neck area which is in the right side of the systems. The zero-velocity curve splits into two branches again when $C_3 < C < C_4$, with the upper branch and lower branch dividing the forbidden region into two parts. Then, increasing C until $C > C_4$ leads that all orbits in the equatorial plane are available.

2.4 Equilibrium points

The equilibrium points of Lundia and Ostro can be easily found where the zero-velocity curves get self-intersected, as shown in Fig. 3. These points represent the locations in space where the particle's velocity and acceleration are both equal to zero. A particle placed there without any initial velocity will keep stationary in the rotating frame. The equilibrium points can be computed by the conditions

$$\frac{\partial U_{sys}(x, y, z)}{\partial x} = \frac{\partial U_{sys}(x, y, z)}{\partial y} = \frac{\partial U_{sys}(x, y, z)}{\partial z} = 0 \quad (17)$$

Tables 3 and 4 give the locations of the equilibrium points of Lundia and Ostro systems and their Jacobi constants respectively. Note that all the data are in normalized form. It can be seen that Lundia system has three collinear points, L_1, L_2, L_3, and two symmetric points L_4 and L_5, while four equilibrium points except for L_1 can be found in the Ostro system. The position of L_1 point can be derived from

Fig. 3 (a) Zero velocity curves of Lundia with five local extreme Jacobi constants. (b) Zero velocity curves of Ostro with four local maximum Jacobi constants

curves around Lundia and Ostro in the equatorial plane respectively. Note that the different colors on the graph represent different values of Jacobi constants for each zero-velocity curve. We can find that one local minimum and four local maximum Jacobi constants ($C_1, C_2 \sim C_5$) exist around Lundia while four local maximum Jacobi constants ($C_2 \sim C_5$) exist around Ostro.

When $C < C_1$ in the Lundia system, the zero-velocity curve is made up of two isolated quasi-circular boundaries which cling to and wrap the two bodies respectively. This restricts a particle can only orbit the primary or the secondary closely. Increasing C to C_1, the two boundaries will connect. It means that a particle orbiting a body have the opportunity to transfer from one of the asteroids to the other one.

When $C_1 < C < C_2$ in the Lundia and $C < C_2$ in the Ostro system, the zero-velocity curve consists of two branches—an inner one that entirely wraps around the two bodies and an outer one that is quasi-circular and far away from the system. It means that the allowable region is di-

Eq. (14) with $y = 0$ and $z = 0$:

$$x_{L_1} = \frac{\mu r_1 E_{a1} - (1-\mu) r_2 E_{a2}}{\mu E_{a1} + (1-\mu) E_{a2} - \omega^2} \quad (18)$$

Substituting the corresponding physical parameters of Ostro in to Eq. (18) can solve that $x_{L_1} = -0.6302$. It can be proved that the L_1 point in the Ostro system is inside of the secondary. In addition, the results also illustrate that all the equilibrium points of both systems are located in the equatorial plane.

The stability of equilibrium points are also discussed because it determines the characteristics of motion of a particle in the vicinity of equilibrium points. The linear stability of the equilibrium points can be judged by the eigenvalues of its state transition matrix Φ. Let us rewrite our dynamic equations Eq. (14) into the following form with six state arguments $X = (x, y, z, \dot{x}, \dot{y}, \dot{z})$, the state transition matrix can be expressed as

$$\Phi = \frac{\partial f}{\partial X}$$

$$= \begin{bmatrix} 0 & 0 & 0 & 1 & 0 & 0 \\ 0 & 0 & 0 & 0 & 1 & 0 \\ 0 & 0 & 0 & 0 & 0 & 1 \\ \omega^2 + U_{xx}^e & U_{xy}^e & U_{xz}^e & 0 & 2\omega & 0 \\ U_{xy}^e & \omega^2 + U_{yy}^e & U_{yz}^e & -2\omega & 0 & 0 \\ U_{zx}^e & U_{zy}^e & U_{zz}^e & 0 & 0 & 0 \end{bmatrix} \quad (19)$$

where $U_{xx}^e, U_{xy}^e, \ldots, U_{zz}^e$ represent the second derivatives of the system potential at the equilibrium point. It is noteworthy that the Roche figure is used to approximate the shapes and physical properties of real binary asteroids 809 Lundia and 3169 Ostro. Under this assumption, the model is symmetric about xy-plane. For convenience, we can reduce the state space to be four-dimensional with ignoring z and $\dot{z}$, and the characteristic equation of the system can be obtained as

$$|\lambda I - \Phi| = \begin{vmatrix} \lambda & 0 & -1 & 0 \\ 0 & \lambda & 0 & -1 \\ -\omega^2 - U_{xx}^e & -U_{xy}^e & \lambda & -2\omega \\ -U_{xy}^e & -\omega^2 - U_{yy}^e & 2\omega & \lambda \end{vmatrix}$$

$$= \lambda^4 + b\lambda^2 + c \quad (20)$$

where

$$b = 2\omega^2 - U_{xx}^e - U_{yy}^e$$

$$c = \omega^4 + \omega^2 (U_{xx}^e + U_{yy}^e) + U_{xx}^e U_{yy}^e - (U_{xy}^e)^2$$

The eigenvalues are now can be obtained

$$\lambda_{1,2} = \pm \sqrt{\frac{-b + \sqrt{b^2 - 4c}}{2}} \quad (21)$$

Table 5 Stability conditions of Lundia system

Stability condition (10^{-4})	L_1	L_2	L_3	L_4	L_5
b	1269.801	20.632	18.434	24.112	24.112
c	−340.281	−0.031	−0.046	0.035	0.035
$b^2 - 4c$	1521.843	0.166	0.218	−0.077	−0.077

Table 6 Stability conditions of Ostro system

Stability condition (10^{-4})	L_1	L_2	L_3	L_4	L_5
b	–	63.576	80.031	19.638	19.638
c	–	−1.837	−1.062	1.334	1.334
$b^2 - 4c$	–	7.753	4.890	−1.688	−1.688

$$\lambda_{3,4} = \pm \sqrt{\frac{-b - \sqrt{b^2 - 4c}}{2}} \quad (22)$$

Recall that if all the eigenvalues are pure imaginary number, i.e. $\lambda^2 < 0$, the corresponding equilibrium point is linear stability. In order to maintain $\lambda^2 < 0$, the coefficients b and c must satisfy

$$\begin{cases} b^2 - 4c > 0 \\ -b \pm \sqrt{b^2 - 4c} < 0 \end{cases} \quad (23)$$

Solve the inequalities Eq. (23) and we can get the linear stability conditions

$$\begin{cases} b = 2\omega^2 - U_{xx}^e - U_{yy}^e > 0 \\ c = \omega^4 + \omega^2 (U_{xx}^e + U_{yy}^e) + U_{xx}^e U_{yy}^e - (U_{xy}^e)^2 > 0 \\ b^2 - 4c = -8\omega^2 (U_{xx}^e + U_{yy}^e) + (U_{xx}^e - U_{yy}^e)^2 \\ \qquad + 4(U_{xy}^e)^2 > 0 \end{cases} \quad (24)$$

The results of the two systems are illustrated in Tables 5 and 6 respectively. It can be seen that none of equilibrium points satisfies Eq. (24), which indicates that all equilibrium points are nonlinear unstable.

3 Periodic orbits and stability

Periodic orbits are the key to understanding the nature of the dynamical system. Moreover, they are also significant for space mission design because they can illustrate the available motion of a spacecraft around the celestial body. In this paper, the global periodic orbits around DSBAs are discussed in detail. The periodic orbits are searched by a numerical method which combines an initial grid searching

and differential correction. If a dynamical system is of the symmetrical characteristic, we can use it to reduce the huge computing workload in searching process by decreasing the in initial searching parameters. On the basis of Hénon's work, the symmetry of the system is discussed firstly.

3.1 Symmetries

Under the Roche figures assumption, the double ellipsoids system is symmetrical about x-axis, xy-plane and xz-plane in geometric properties. It can be derived from the symmetries that the equation of motion Eq. (14) is invariant under the transformation S

$$S : (x, y, \dot{x}, \dot{y}, t) \rightarrow (x, -y, -\dot{x}, \dot{y}, t)$$

Applying S to a planar periodic orbit can obtain that it is also symmetrical about x-axis. Based on the planar periodic orbit, the spatial ones are generated as follows. The planar x-axis symmetric orbit crosses the x-axis perpendicularly twice, at two points P and Q respectively. Let $\Delta z_0, \Delta \dot{z}_0$ be the vertical perturbation at some crossing in P; $\Delta z_1, \Delta \dot{z}_1$ the perturbation at the next crossing in Q; and $\Delta z_2, \Delta \dot{z}_2$ the perturbation at the following crossing, which will be again in P. According to the Hénon's work (1973), the relation of these various perturbations can be expressed as

$$
\begin{bmatrix} \Delta z_1 \\ \Delta \dot{z}_1 \end{bmatrix} = \begin{bmatrix} A & B \\ C & D \end{bmatrix} \begin{bmatrix} \Delta z_0 \\ \Delta \dot{z}_0 \end{bmatrix},
$$
$$
\begin{bmatrix} \Delta z_2 \\ \Delta \dot{z}_2 \end{bmatrix} = \begin{bmatrix} A' & B' \\ C' & D' \end{bmatrix} \begin{bmatrix} \Delta z_1 \\ \Delta \dot{z}_1 \end{bmatrix}
$$

(25)

and

$$A' = D, \qquad B' = B, \qquad C' = C, \qquad D' = A$$

If $B = 0$ and a perturbed orbit have the initial condition $\Delta z_0 = 0, \Delta \dot{z}_0 = \varepsilon$ (ε can be arbitrarily chosen), from Eq. (25), we have

$$\Delta z_1 = 0, \qquad \Delta \dot{z}_1 = D\varepsilon, \qquad \Delta z_2 = 0, \qquad \Delta \dot{z}_2 = \varepsilon$$

It means the perturbed orbit closes back to its initial position in phase space. Because of the invariant of z_1, z_2 and the change of $\dot{z}_1, \dot{z}_2$, the spatial orbit is also symmetrical with respect to x axis.

Similarly, if $C = 0$ and the initial condition is $\Delta z_0 = \varepsilon, \Delta \dot{z}_0 = 0$, we find

$$\Delta z_1 = A\varepsilon, \qquad \Delta \dot{z}_1 = 0, \qquad \Delta z_2 = \varepsilon, \qquad \Delta \dot{z}_2 = 0$$

It means the orbit is symmetrical with respect to xz-plane.

For the case $A = 0$ and a perturbed orbit have the initial condition $\Delta z_0 = 0, \Delta \dot{z}_0 = \varepsilon$ we have

$$\Delta z_1 = 0, \qquad \Delta \dot{z}_1 = C\varepsilon, \qquad \Delta z_2 = -\varepsilon, \qquad \Delta \dot{z}_2 = 0$$

then we continue the motion after one revolution which is symmetrical of the initial state with respect to xy-plane, we have

$$\Delta z_3 = 0, \qquad \Delta \dot{z}_3 = -C\varepsilon, \qquad \Delta z_2 = \varepsilon, \qquad \Delta \dot{z}_2 = 0$$

where $\Delta z_3, \Delta \dot{z}_3$ and $\Delta z_4, \Delta \dot{z}_4$ are the vertical perturbations at P and Q in the secondary revolution respectively. It means that the orbit is periodic and has the doubly-symmetrical characteristic which enjoys the xy-planar symmetry and x-axis symmetry.

From the discussion above, one type of planar symmetrical periodic orbit and three types of spatial symmetrical periodic orbits can be found in the system. The symmetries of the periodic orbits are the valuable characteristics, and can be used to reduce the initial searching parameters in the searching process, which is discussed in detail in the next section.

3.2 Global searching

The global searching method targets to find large-scale periodic solutions for the symmetrical and non-integrable systems in a given meshed region of initial conditions. System (14) indicates that a periodic orbit corresponds to a six-dimensional state $(x, y, z, \dot{x}, \dot{y}, \dot{z})$ at the initial conditions and a period T, which can be regarded as the searching parameters. The symmetrical characteristic of the periodic orbits can be used to reduce the initial conditions to four-dimensional subspaces at least. Taking the planar and spatial x-axis symmetrical periodic orbits for examples, the global searching procedure is introduced as follows.

The search parameters are implemented in a triple grid $(x_0, \dot{y}_0, \dot{z}_0)$. The system (14) is integrated numerically with every neighboring mesh point in a given region using a step-seventh-to eighth-order Runge-Kutta method. Since the periodic orbits are symmetrical, they will trace a mirror image and re-encounter the x-axis with $t = T/2$. Therefore, the xz-plane can be set as a Poincaré section. The integration terminates when the orbit encounters with the Poincaré section. The final state of the orbit on the Poincaré section is

$$\mathbf{x}_f = (x_{T/2}, 0, 0, \dot{x}_{T/2}, \dot{y}_{T/2}, \dot{z}_{T/2})$$

an orbit is periodic if the conditions $z_{T/2} = 0$ and $\dot{x}_{T/2} = 0$ are satisfied. For every mesh point $(x_0, \dot{y}_0^j, \dot{z}_0^k)$, $(j, k = 1, 2, \ldots, n)$, we define two intervals $I_1 = (z_{T/2}^j, z_{T/2}^{j+1})$ and $I_2 = (\dot{x}_{T/2}^k, \dot{x}_{T/2}^{k+1})$. Only the occurrences of both $z_{T/2}$ and $\dot{x}_{T/2}$ switching signs in I_1 and I_2 meanwhile can indicate the existence of a periodic orbit, as shown in Fig. 4.

For a given x_0, the $\{\dot{y}_0, \dot{z}_0\}$ space is searched. In general, the solutions appear as points in the $\dot{y}_0 \dot{z}_0$-plane. This process is repeated for a sufficient number of x_0 values. When all the solutions are plotted in the spatial $\{x_0, \dot{y}_0, \dot{z}_0\}$ space, families

of solutions appear as planar lines. For a slice of constant x_0, Fig. 5 illustrates the interior mesh points in the $\dot{y}_0\dot{z}_0$-plane and example periodic solutions.

Russell (2006) proposed a 'six-step method' to find the periodic solutions in the interior mesh grid. However, this method requires great refinement mesh, which will lead the significant increase of the computing workload. In this paper, the mesh grids are divided into three cases in detail by the distributions of the periodic solutions. The nearest-solution criteria for the three cases are established to approximate the initial conditions of periodic orbits as follows.

Case 1: The two boundaries intersect four different lines of a mesh in the $\dot{y}_0\dot{z}_0$-plane, as shown in Fig. 5(a). The nearest solution is selected at the center of the mesh.

Case 2: The two boundaries intersect three lines of a mesh in the $\dot{y}_0\dot{z}_0$-plane, as shown in Fig. 5(b). The black diamonds in Fig. 6(b) indicate the crossing points of which a line is intersected by both boundaries. Using the bisection
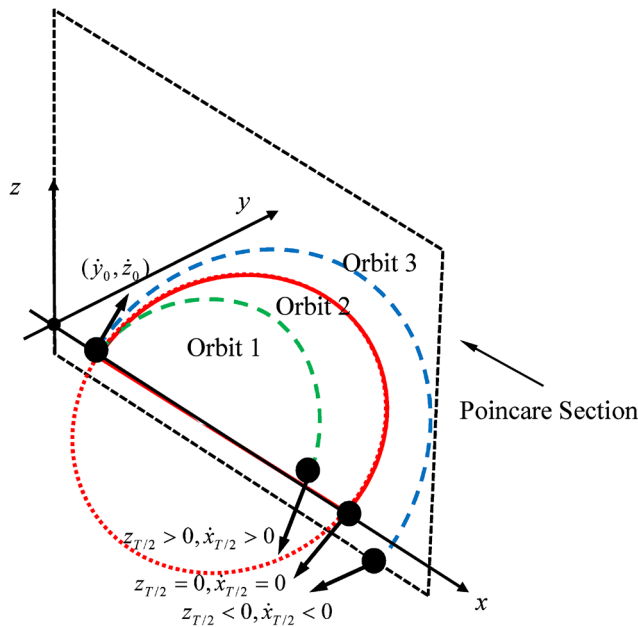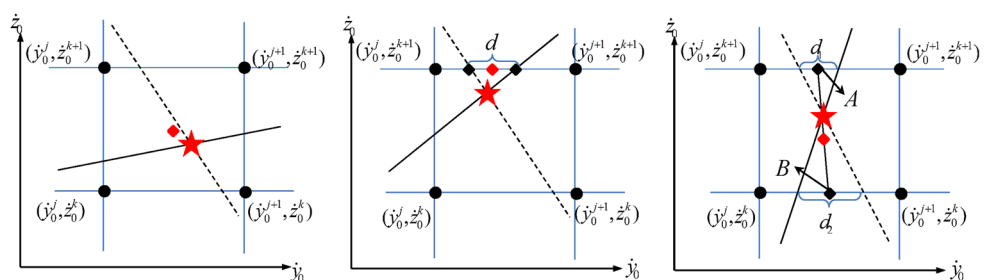
method developed by Vrahatis and Iordanidis (1986) when only the change of sign for $\dot{x}_{T/2}$ or $\dot{z}_{T/2}$ is focused on, the coordinates of these points can be computed. The nearest solution is selected at the midpoint of the segment which is connected by the two crossing points.

Case 3: The two boundaries intersect only two lines of a mesh in the $\dot{y}_0\dot{z}_0$-plane, as shown in Fig. 5(c). The two boundaries intersect the lines and form two segments, d_1 and d_2. Note that the coordinates of the endpoints of the two segments are also computed by the bisection method. We record the midpoints of the two points as A and B. The solution is located at the center of the segment AB.

The errors still exist even the nearest solutions are found by the presented approach. Hence, a local differential corrector is applied to target the accurate initial conditions of periodic orbits. The differential corrector of the spatial x-axis symmetrical orbits attempts to remove the unwanted $z_{T/2}$ and $\dot{x}_{T/2}$ by adjusting $\dot{y}_0$ and $\dot{z}_0$. In the meanwhile, x_0 should be kept constant. The iteration equation can be expressed as

$$\begin{bmatrix} \tilde{\delta}\dot{y}_0 \\ \tilde{\delta}\dot{z}_0 \end{bmatrix} = \begin{bmatrix} \Phi_{z\dot{y}} - \dot{z}\Phi_{y\dot{y}}/\dot{y} & \Phi_{z\dot{z}} - \dot{z}\Phi_{y\dot{z}}/\dot{y} \\ \Phi_{\dot{x}\dot{y}} - \ddot{x}\Phi_{y\dot{y}}/\dot{y} & \Phi_{\dot{x}\dot{z}} - \ddot{x}\Phi_{y\dot{z}}/\dot{y} \end{bmatrix}_{T/2}^{-1} \begin{bmatrix} -z_{T/2} \\ -\dot{x}_{T/2} \end{bmatrix}$$

The iteration process is continued until the conditions $|z_{T/2}| < 10^{-10}$ and $|\dot{x}_{T/2}| < 10^{-10}$ are satisfied meanwhile. Generally, only three or four iterations are required. The corrected initial conditions can be considered as the accurate periodic solutions for spatial x-axis symmetrical orbits.

To obtain the planar periodic orbits, one of the initial conditions z_0 is set to be zero, and then the searching procedure can be simplified to a bisection method. For the xz-plane symmetrical and doubly symmetrical spatial periodic orbits, the searching procedure of global periodic orbits is similar with the case of spatial x-axis symmetry. However, the changes occur on the initial searching parameters, the cut-off time and the periodic conditions, as illustrate in Table 7. Their corresponding differential correctors are also adjusted according to the symmetrical characteristics.

3.3 Families and stability

The large-scale periodic orbits around 809 Lundia and 3169 Ostro are searched by using the aforementioned approach,

Fig. 4 Illustration of the x-axis symmetrical periodic orbits. Note that the orbit 1 starts with the initial conditions $(x_0, \dot{y}_0^j, \dot{z}_0^k)$, orbit 3 starts with the initial conditions $(x_0, \dot{y}_0^{j+1}, \dot{z}_0^k)$ or $(x_0, \dot{y}_0^j, \dot{z}_0^{k+1})$, while orbit 2 is the periodic orbit

Fig. 5 Interior mesh grid in $\dot{y}_0\dot{z}_0$-plane at a given x_0. Notes, the *dash line* is the boundary which $\dot{x}_{T/4}$ switches sign, the *solid line* is the boundary which $\dot{z}_{T/4}$ switches sign. The *red pentangle* and the *red diamond* indicate the periodic solution and the nearest solution to the periodic one respectively
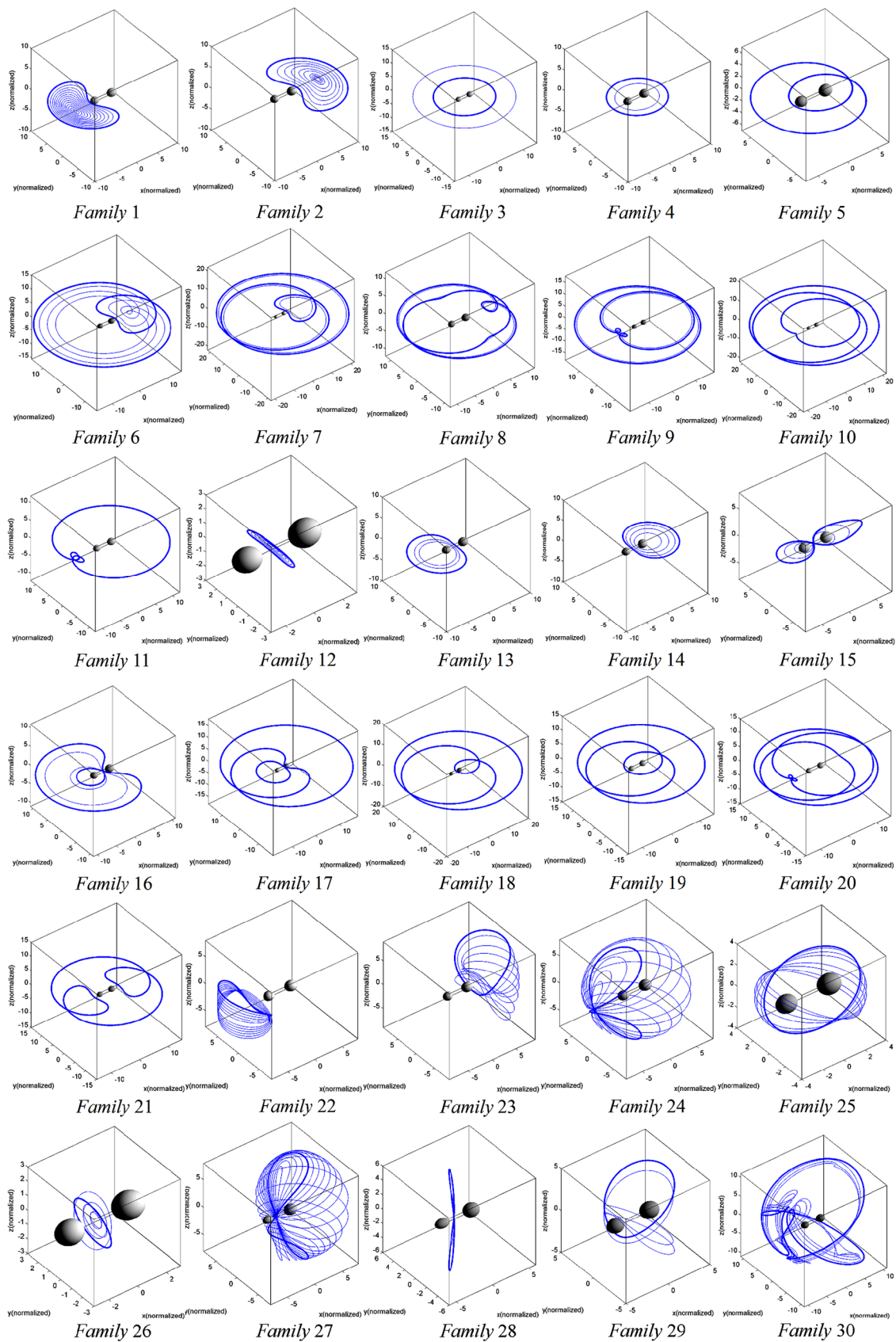
Fig. 6 Periodic orbits of 30 families around Lundia system varying as the Jacobi constant of the corresponding range, shown in the *bod-fixed frame*. The *shadowed ellipsoids* indicate the shapes of Lundia and the *bold line* indicates a representative orbit of each family

Table 7 Searching parameters for different symmetrical periodic orbits

	Planar	x-axis symmetry	xz-plane symmetry	Doubly symmetry
Initial conditions	$(x_0, \dot{y}_0)$	$(x_0, \dot{y}_0, \dot{z}_0)$	$(x_0, z_0, \dot{y}_0)$	$(x_0, \dot{y}_0, \dot{z}_0)$
Poincaré section	xz-plane	xz-plane	xz-plane	xz-plane
Cut-off time	$T/2$	$T/2$	$T/2$	$T/4$
Periodic conditions	$\dot{x}_{T/2} = 0$	$z_{T/2} = 0, \dot{x}_{T/2} = 0$	$\dot{x}_{T/2} = 0, \dot{z}_{T/2} = 0$	$\dot{x}_{T/4} = 0, \dot{z}_{T/4} = 0$

respectively. A $10 \times 10 \times 10$ cubic in the both systems in configuration space are selected as the search regions. It is noted that all the values are normalized form. The period T can be replaced by the integer-value N because the terminal conditions for all orbits occur at xz-plane crossing. Thus for a given initial condition, the trajectory is integrated forward and terminated on the Nth crossing of the xz-plane. For the final run, $N_{\max}$ is chosen to be 3 of the planar case and to be 1 of the spatial case. Finally, over 186000 grid points are evaluated in the both systems. 94163 solutions of the Lundia and 89013 solutions of the Ostro are found spending approximately 23 hours of total computer time on Intel Core i5 PC with 3.20 GHz processors. According to the topological structures in the configuration space of the periodic orbits, the results can be classified to 30 families orbits exist around Lundia and 29 families exist around Ostro. These periodic orbit families distributed on different ranges of Jacobi constant are shown in Figs. 6 and 7.

The results show the diversity of periodic orbits in the both systems. These periodic orbits can be distinguished by morphology preliminarily. It can be found that both the commonness and distinction of periodic orbits exist in the two systems. A total of 15 families which have similar morphology exist in the both systems. These families can be divided into five classifications: the periodic orbits near equilibrium points $L_{2,3}$ including the Lyapunov and Halo orbits (Families 1–2, Families 22–24 of Lundia and 18–20 of Ostro); the retrograde and prograde quasi-circular orbits (Families 3, 4); the double-circle orbits in the equatorial plane (Family 5); the quasi-circular periodic orbits which contact or encircle the collinear points (Families 6–11); and the spatial quasi-circular orbits (Family 25 of Lundia and 21 of Ostro). In addition, although the morphology of Family 21 of Lundia and Family 17 of Ostro are obvious different, both of the families are quasi-symmetrical to yz-plane about themselves.

Due to the existence of L_1, some families of periodic orbits can only be found in the Lundia system: The Lyapunov (Families 12, 27, 28 of Lundia) and Halo (Family 26 of Lundia) orbit near L_1 are found in Lundia system. Some quasi-circular orbits which encircle one body of the binary (Families 13 and 14 of Lundia) and '8' formal orbits which revolve around both bodies (Family 15 of Lundia) also exist. In addition, the periodic orbits of Families 16–18, which pass through the gap between the two bodies, can only be found in the Lundia system.

It is interesting that a number of specific quasi-circular periodic orbits which encircle $L_{4,5}$ (Families 12–15, 23–24 of Ostro) only exist around Ostro. Families 23 and 24 can be considered as the Families 12 and 13 added a vertical mode of motion. Moreover, some periodic orbits around Ostro are more complex than around Lundia. The shapes of Ostro (two bodies get much closer) lead to the special gravitational field near y-axis, which may be the main causes to generate these periodic orbits.

The stability of periodic orbits is deserved to be paid attention because it also relates to the motion of a particle on the orbit. If a periodic orbit is stable, the trajectory keeps its original location and will not diverge exponentially. If a periodic orbit is unstable, the trajectory will diverge exponentially from the orbit and wander over a region of phase space in general. According to the Floquet theory, the stability of periodic orbits is determined by the nature of the state transition matrix. Koon et al. (2000) proved that the matrix is symplectic for the systems and their eigenvalues λ_i have the form $\{\lambda, \lambda^{-1}, \bar{\lambda}, \bar{\lambda}^{-1}, 1, 1\}$. On the basis of the eigenvalues, a single, real scalar instability index is proposed in Eq. (26)

$$\rho = \max_{1 \leq j \leq 6} |\lambda_j| \qquad (26)$$

This index can judge the stability of periodic orbits and measure how far a particular unstable orbit is from the stability boundary. If $\rho > 1$, the periodic orbit is unstable while $\rho \leq 1$ the periodic orbit is stable. The instability index ρ of the periodic orbits varying with Jacobi constants are calculated. The stability curves are shown in Fig. 8.

The stability curves of the periodic orbits around Lundia are shown in Fig. 8(a). According to the distributions of the instability indexes and Jacobi constants of the periodic orbits, the families of periodic orbits can be divided into four classes. Nearly half of the families (46 %) concentrate on a small range of Jacobi constants ($-0.25 \sim -0.1$) and they are defined as Class 1. It is noted that these families have low instability indexes. Although the Jacobi constants of Families 8, 9, 11, 15, 20 and 21 also lie in the range roughly same as that of Class 1, they are classified as Class 2 because of the high instability indexes. In other words, these orbits will diverge exponentially when perturbed. The stable periodic
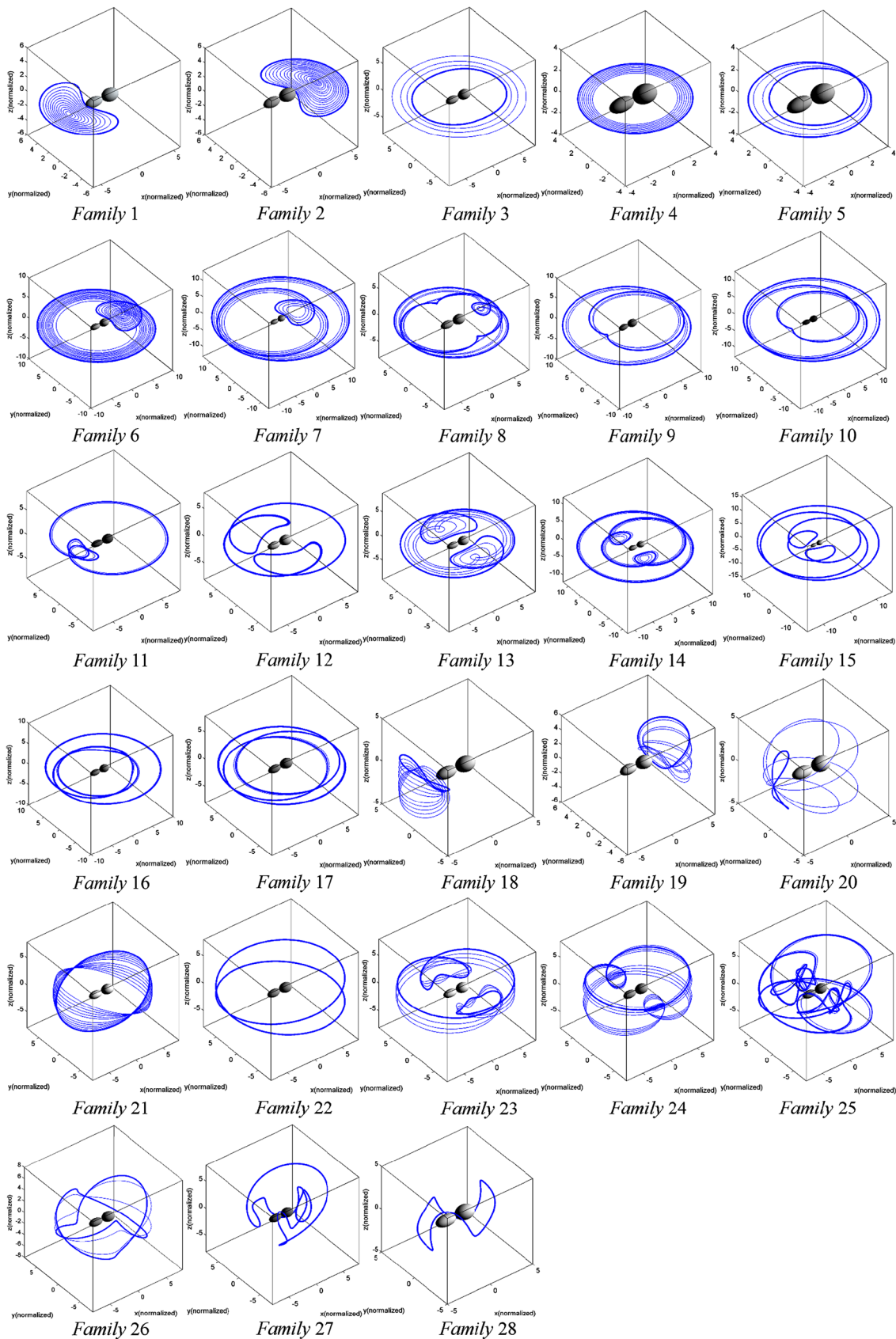
Fig. 7 Periodic orbits of 28 families around Lundia system varying as the Jacobi constant of the corresponding range, shown in the *bod-fixed frame*. The *shadowed ellipsoids* indicate the shapes of Ostro and the *bold line* indicates a representative orbit of each family
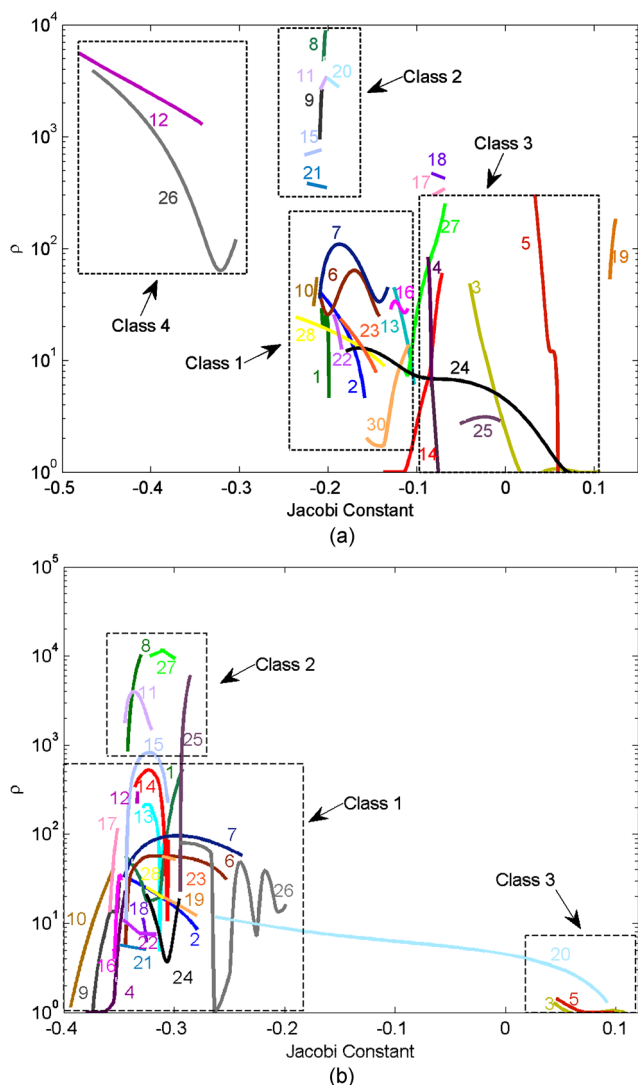
Fig. 8 (a) The stability curves of Lundia. (b) The stability curves of Ostro

orbits can be found in the Class 3 which includes the retrograde and prograde quasi-circular orbits (Families 3 and 4), the double-circle orbits in equatorial plane (Family 5), and the vertical Lyapunov orbits near L_3 (Family 24). It is noted that all the stable periodic orbits have relative high energy levels. Class 4, including the Lyapunov and Halo orbits near L_1 (Families 12 and 26), is a special class that only exist in Lundia system. These periodic orbits have high instability indexes as well as low energy levels.

The stability curves of Ostro system (Fig. 8(b)) are quite different from Lundia. It can be seen that three main classes of periodic orbits are classified. Class 1 contains larger portion of families (about 78 %) varying as the Jacobi constants from −0.4 to −0.2. The periodic orbits with high instability indexes also can be found in Class 2, which contains Families 8, 11, 25 and 27. It is noteworthy that the complex morphology always means that the periodic orbit has

high instability index. Only the prograde quasi-circular orbits (Families 3), the double-circle orbits in equatorial plane (Family 5), and the vertical Lyapunov orbits near L_3 (Family 20) are stable and they are classified as Class 3. Similar with the case in the Lundia system, the stable orbits are also of high energy level.

3.4 Invariant manifold structures

In the following, the invariant manifolds associated with periodic orbits are discussed to gain further insight into the dynamical nature and the potential applications. The invariant manifold is a multidimensional surface embedded in the whole phase space of the system, and orbits starting on the surface will always remain on that same surface (Baoyin and McInnes 2006). The computation of the stable and unstable manifolds associated with periodic orbits can be accomplished numerically. The nonlinear differential equations Eq. (14) is linearized to get the equation $\dot{\mathbf{X}} = A\mathbf{X}$, where A is the coefficient matrix and has eigenpairs (λ_i, v_i). The linear space spanned from vector v_i with positive or negative real part is called the unstable or stable manifold respectively (Gong et al. 2007). It is assumed that X_0 is a point on the periodic orbit, Then the stable eigenvector $Y^s(X_0)$ and unstable eigenvector $Y^u(X_0)$ of A is easy to get. The initial conditions of the stable and unstable manifold at X_0 can be obtained as

$$X^s(X_0) = X_0 \pm \varepsilon Y^s(X_0)$$

$$X^u(X_0) = X_0 \pm \varepsilon Y^u(X_0)$$

Note that ε is a small displacement from X_0 (about the value of 10^{-6} in normalized form in this paper). The dynamical system (14) is then integrated with these initial conditions to obtain the unstable and stable manifolds. The stable and unstable manifolds of all unstable periodic orbits presented in Sect. 3.4 are computed. We find that the distributions of the invariant manifolds of most periodic orbits are chaotic in the configuration space, however, except for the Families 1, 2, 12, 26 of Lundia and the Families 1, 2 of Ostro.

As shown in Fig. 9, the stable and unstable manifolds of the periodic orbits of Family 12 around Lundia link the surfaces of the primary and the secondary. These trajectories on the manifolds are propagated for approximately 5 hours. The similar spatial tube-like structures generated from the invariant manifolds of the Family 26 also exist around Lundia. On the basis of the characteristics, a particle has the opportunity to launch from one body to the periodic orbit guided by the stable manifolds and then land on the other body guided by the unstable manifolds, which is discussed in detail in the next section.

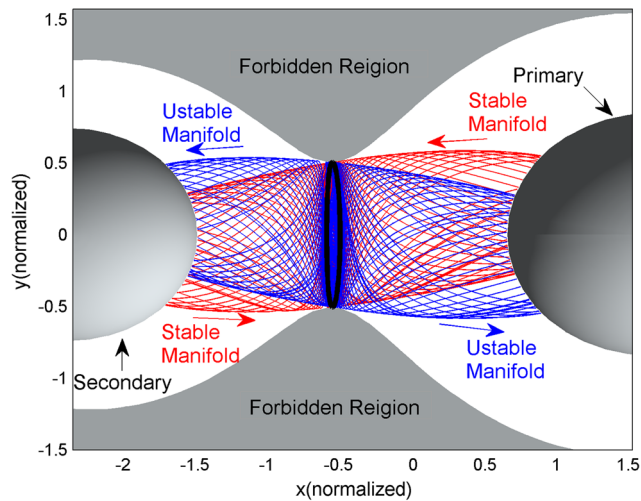The stable and unstable manifolds of the periodic orbits of Families 1 (the Lyapunov orbits near L_2) around

Fig. 9 The stable (*red*) and unstable (*blue*) invariant manifolds of a Lyapunov orbit near L_1 around Lundia that has a Jacobi constant of -0.4813
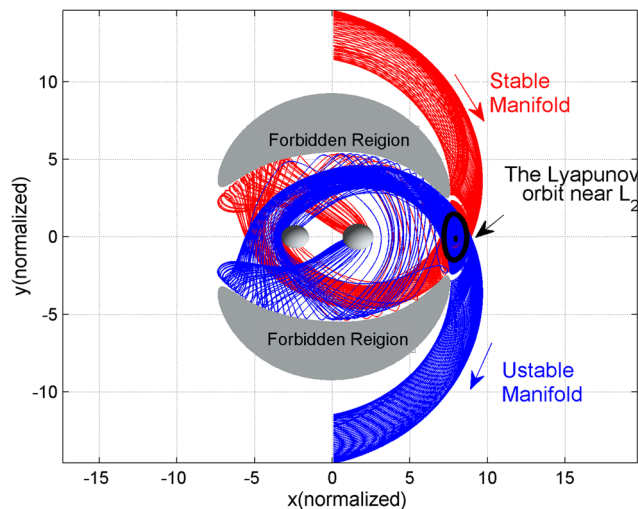

Fig. 10 The stable (*red*) and unstable (*blue*) invariant manifolds of a Lyapunov orbit near L_2 around Lundia that has a Jacobi constant of -0.2076

Lundia systems are shown in Fig. 10, which also present the planar tube-like structures. The motion of a particle on these invariant manifolds can be divided into three types: approaching the surface of one body directly; reaching the surface of the other body after reflecting on the zero-velocity surface; and escaping to the outer region. It is noteworthy that the stable and unstable manifolds of the Family 2 around Lundia and the Families 1 and 2 around Ostro also present the similar characteristics. Based on the characteristics, we can carry out a ballistic landing for a spacecraft using the unstable manifolds, which is discussed in the next section.

4 Applications to space mission

The periodic orbits described above may offer a variety of possible applications to space missions. Due to the morphology and stable characteristics, some quasi-circular orbits can provide the potential applications for scientific space observation. Because the invariant manifolds of the planar Lyapunov and Halo orbits near collinear points intersect the surface of one or both asteroids, they can be used to approach the surface of asteroids and transfer between two bodies. According to Yu's work (2014), the radiuses of the globular region where the orbital motion near the asteroid is dominated by its own gravitational field can be obtained as 5.31 km of Lundia and 2.05 km of Ostro respectively. Both of the radiuses are smaller than the dimensions of most of the periodic orbits. Indeed, the motion of a spacecraft on the periodic orbits will be affected by the perturbations such as radiation pressure and the gravitational field of the Sun. However, it is that the dynamical behavior based mainly focused on in this paper, which may provide some valuable references for the real space mission designs.

4.1 Space observation

To enhance our knowledge of the DSBAs, it is necessary to carry out the lone-time space observation to the bodies. In this section, we discuss whether some periodic orbits are appropriate to be used to observe the binary system. Considering the diversity of the periodic orbits, it is complicated for us to select the suitable periodic orbits for observation. To do this, we define three criteria for choosing and assessing a periodic orbit.

1. The orbit should revolve around one or both bodies at least once.
2. The period of the orbit is less than 2 days.
3. The instability index of the orbit should satisfy $1 \le \rho \le 50$.

Criterion 1 ensures the spacecraft to observe the entire asteroids. Criterion 2 limits the period to be an acceptable value for the observation. Criterion 3 indicates how sensitive the orbit is to perturbations. Generally, station-keeping costs are small if an orbit has low instability index or is stable. According to the defined criteria, the periodic orbits of Families 3–5, 13–14, 25 around Lundia and Families 3–5, 21 around Ostro can be chosen as the candidates for the observation mission.

The distance between the asteroids and the spacecraft is a significant factor for high resolution about the asteroids. Hence it can be used to characterize the observation ability of a periodic orbit. r_{p1} and r_{p2} indicate the distances between the spacecraft and the primary or the secondary respectively.
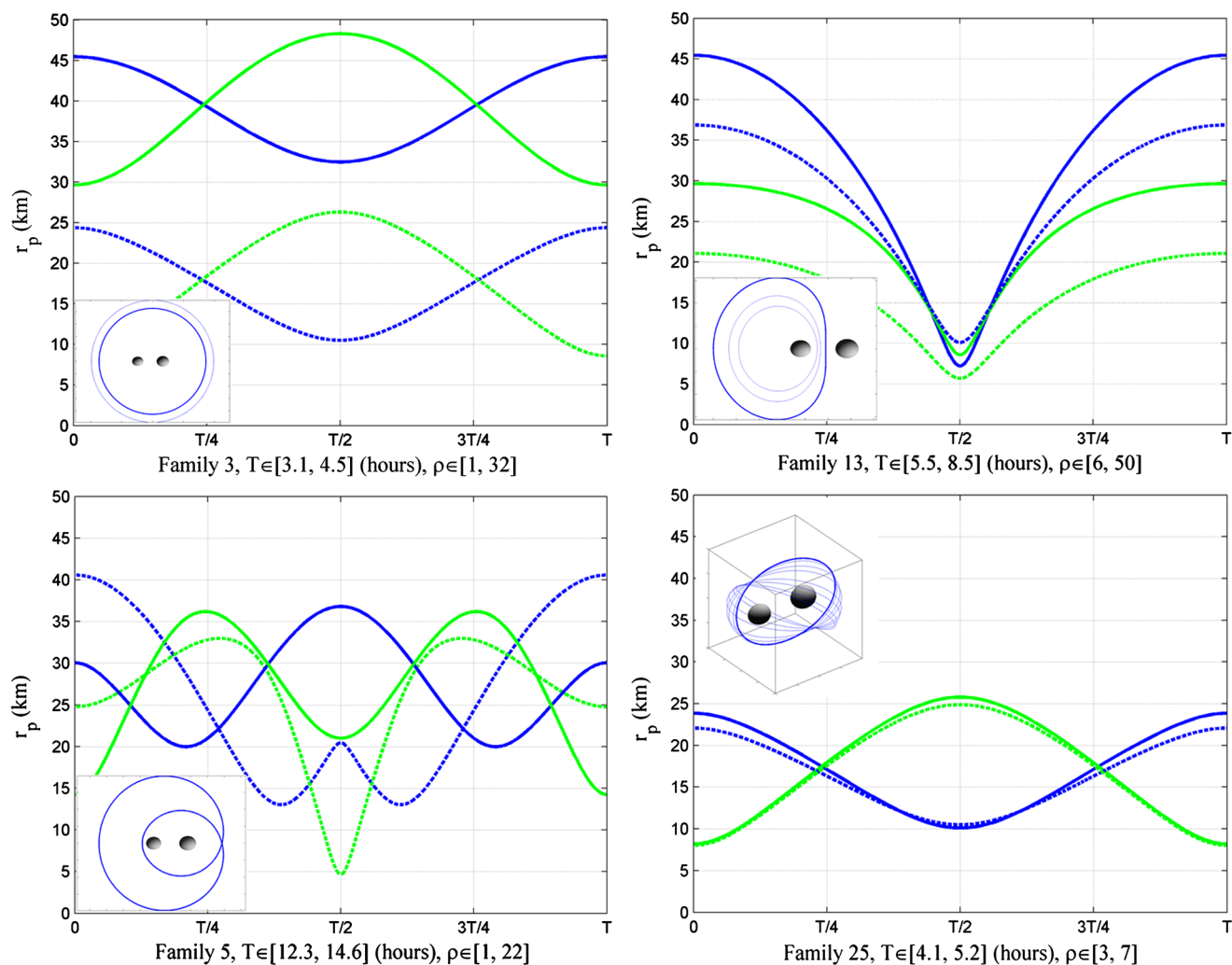
Fig. 11 The distance curves of some periodic orbits around Lundia

Varying as the period of an orbit in the Lundia system, the distances to the primary and the secondary appear as the blue and green curves respectively, as shown in Fig. 11. Note that the analysis for the Ostro system is similar. The two borderline periodic orbits with the largest and smallest Jacobi constants in a family, which are indicated by the solid and dash lines respectively, are selected to assess the observation abilities of the family.

According to the distance curves, these periodic orbits can be used to carry out four kinds of observation missions. The periodic orbits of Families 3 and 4 are appropriated to be used to observe the global system because the distances to the primary are almost equal to the corresponding distances to the secondary. The distance curves of the periodic orbits of Family 13 are shown in Fig. 11(b), it can be easily seen that the distance to the secondary keeps closer than it to the

primary. Hence these periodic orbits are suitable to observe the secondary. Similar, the periodic orbits of Family 14 are suitable to observe the primary. The distance curves of the double-circle orbits are shown in Fig. 11(c). The distance to the secondary is much closer than it to the primary at the time T/2. In the rest of time, the minimum and maximum distances to both bodies are almost equal. That is to say, the double-circle orbits (Family 15) can not only obtain the global information about the system, but also carry out the observation to the secondary especially. The distance curves of the spatial quasi-circular orbits are similar to the planar cases, as shown in Fig. 11(d). However, a spacecraft on the orbits can observe higher or lower latitude region of the surface. Moreover, although the periodic orbits of Families 23 and 24 are of the relatively long period, they can also carry out the three-dimensional observation to the global system of Ostro.

4.2 Ballistic landing

Because of the weak gravitational field of the asteroids, it is possible for a spacecraft to carry out the ballistic landing on the surface of bodies. According to the aforementioned invariant manifold structures, one can easily see that the unstable manifolds of the periodic orbits of Families 1, 2 around both systems intersect the surfaces of two bodies. Therefore, these unstable manifolds may offer the fuel-free trajectories to approach the surface of the asteroids. The example of the periodic orbits of Family 2 (The Lyapunov orbits near L_2) around Lundia and Ostro are illustrated in Fig. 12. Two
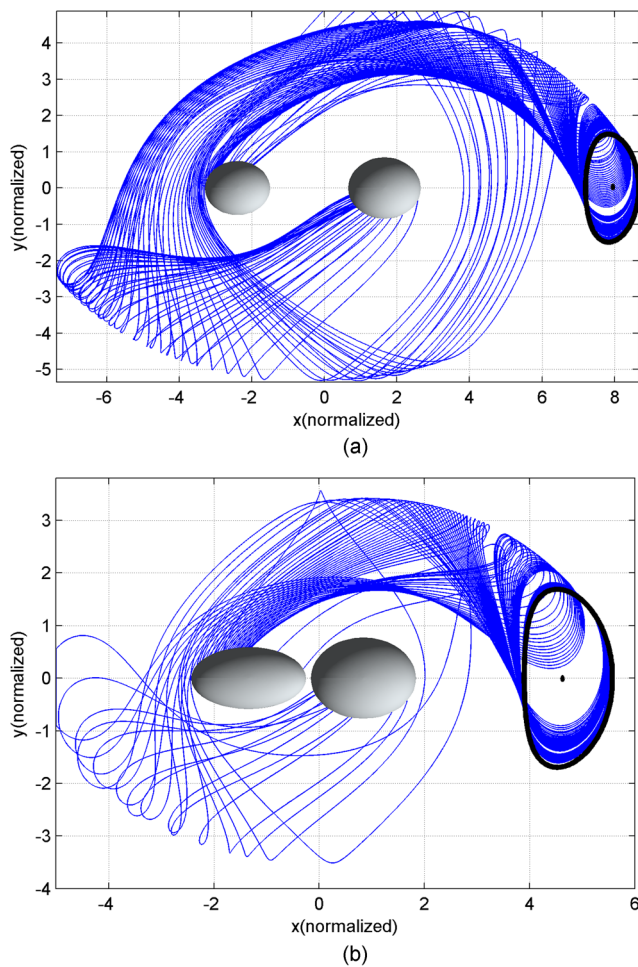

Fig. 12 The unstable manifolds of the planar Lyapunov orbits near L_2 near Lundia (**a**) and Ostro (**b**)

types of the ballistic landing trajectories can be found: the direct trajectories to the secondary and the indirect trajectories to the primary. It is noteworthy that the dimensions of the landing trajectories are out of the range of the aforementioned globular region. In fact, the perturbations should be taken into consideration and will affect the landing trajectories which are obtained in our systems. However, in this paper these trajectories can be regarded as a guide role for the real landing mission design. Consequently, a spacecraft has the opportunities to land on the surface of both bodies guided by these unstable manifolds.

A lander with large speed would most likely bounce back and even escape after hitting the surface. Hence it is necessary to analyze the landing velocity to find out whether the braking manoeuver is required for safety landing. The average longest axis of two bodies is defined as the characteristic radius of the system. Then the escape velocity of the system can be computed by the characteristic radius and the total mass of two bodies. We obtain v_{escape} is 2.9368 m/s of Lundia and is 1.7533 m/s of Ostro. Bellerose and Scheeres (2008b) proposed that the lander will slightly deform from the impact with the asteroid and have a coefficient of restitution between 0 and 1. It means that the energy consumption of a spacecraft will occur in the landing process. Therefore, the velocity after impact is less than the landing velocity. The largest landing velocities of the direct and indirect trajectories are demonstrated in Table 8. One can easily see that both the landing velocities of the Lundia and Ostro systems are less than their corresponding escape velocities respectively. Hence, the unstable manifolds of the Lyapunov orbits near $L_{2,3}$ are able to provide the fuel-free to achieve the ballistic landing to the surface of the asteroids.

4.3 Ballistic transfer

To detect the inner structures of both bodies of DSBAs on site or take samples return to the earth, the spacecraft should be given the ability to transfer between two bodies. As discussed in Sect. 3.4, the stable and unstable manifolds of the periodic orbits of Family 12 and 26 provide the 'conduits' to connect the two bodies of the Lundia system. Thus a spacecraft can be guided by the stable manifolds to reach the periodic orbit from the asteroid, and then land on the other asteroid guided by the unstable manifolds. In this section,

Table 8 The largest landing velocities of direct and indirect trajectories varying as the Jacobi constants

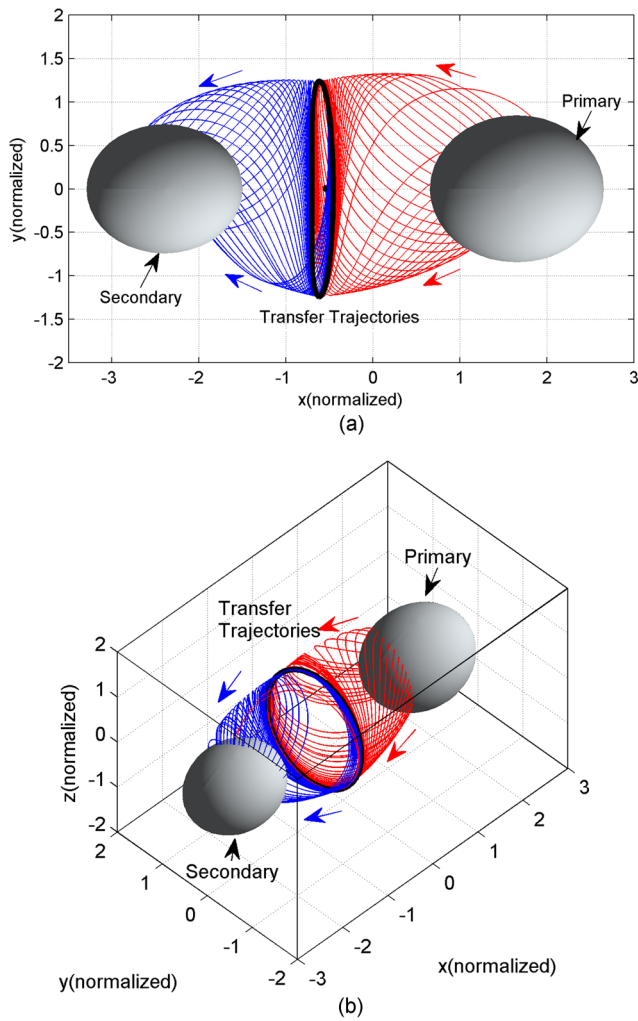|	Velocity (m/s)	$C = -0.2088$	$C = -0.2076$	$C = -0.2064$
Lundia	Direct Trajectory	–	2.9282	2.9310
	Indirect Trajectory	2.9068	2.9137	2.9293
Ostro	Direct Trajectory	1.7093	1.7184	1.7391
	Indirect Trajectory	1.7092	1.7157	1.7321

Fig. 13 The transfer trajectories guided by the stable and unstable manifolds of the planar (**a**) and spatial (**b**) Lyapunov orbits near L_1 around Lundia
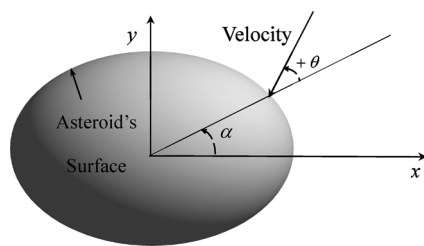

Fig. 14 Illustration showing location and orientation of velocity vector as it intersects the surface

Fig. 15 The launching and landing velocities varying as their corresponding areas. (**a**) Transfer from the primary to the secondary. (**b**) Transfer from the secondary to the primary

the major parameters of the planar and spatial transfer trajectories, including the launching area, the landing area and velocity are discussed.

For the planar cases, the transfer trajectories from the primary to the secondary are shown in Fig. 13(a) for instance. Specifying the Jacobi constant gives the velocity magnitude for each trajectory, whereas the location of the trajectory and
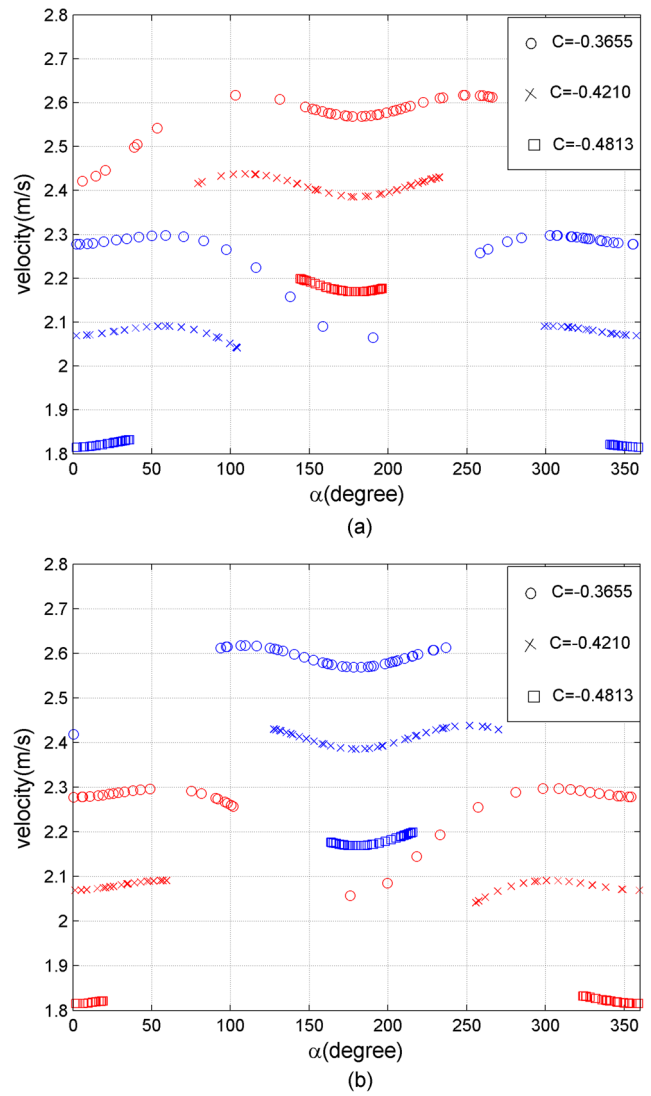
the orientation of the velocity are specified using α and θ, as shown in Fig. 14. The variable α corresponds to the location of the transfer trajectory on the surface of an asteroid, and θ indicates the direction of landing velocity.

Figure 15 illustrates the landing and launching areas varying as α at different energy levels. It is noted that Fig. 15(a) demonstrates the transfer trajectories from the primary to the secondary while Fig. 15(b) shows the trajectories from the secondary to the primary. The color coded red to indicate the stable manifolds and the blue dots indicate the unstable manifolds. In addition, the different Jacobi constants are represented by the different symbols. The landing areas on the primary and the launching areas on the secondary are grouped mainly from $\alpha = 100°$ to $\alpha = 250°$, namely, the left side of the body. On the other hand, the launching areas of the primary and the landing areas of the
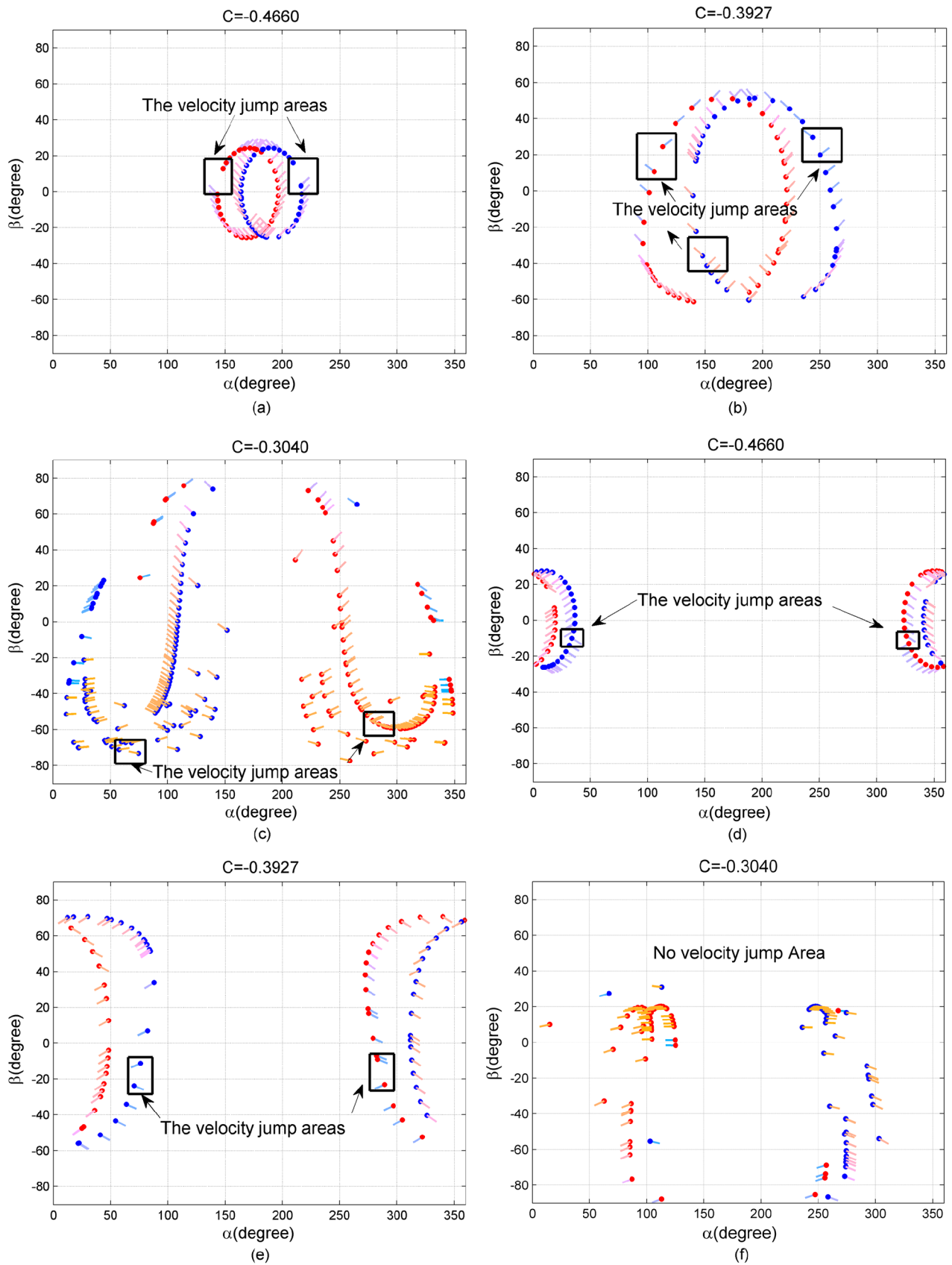
Fig. 16 The launching and landing areas as well as velocities of spatial transfer trajectories varying as the Jacobi constants. Note that the (**a**) ∼ (**c**) and (**d**) ∼ (**f**) belong to the primary and the secondary respectively

Table 9 The areas with the lowest landing velocity on the surface of asteroids

		$C = -0.3040$	$C = -0.3927$	$C = -0.4660$
Primary	(α, β) (degree)	(331.6, 0.8)	(220.8, 0.6)	(196.1, 2.0)
	Velocity (m/s)	2.63	2.48	2.24
Secondary	(α, β) (degree)	(125.3, −1.8)	(50.1, 3.2)	(19.3, −1.4)
	Velocity (m/s)	2.37	2.15	1.86

secondary concentrate on from $\alpha = 0°$ to $\alpha = 80°$ and $\alpha = 280°$ to $\alpha = 360°$, or the right side of the body. As the energy level increases, the invariant manifolds are shown to provide the growing-larger coverage of landing and launching. The landing velocity keeps from 1.8112 m/s to 2.6324 m/s varying as different Jacobi constants, as shown in Fig. 15. Apparently, the spacecraft guided by the invariant manifolds is unable to escape from the system when landing on the surface of the body. Furthermore, the lowest landing velocities can be found at the equator and opposite of binary alone x-axis. Therefore, if we intend to minimize the impact effect of a spacecraft as much as possible, the areas near the equator are the suitable selection.

The planar transfer trajectories provide a convenient framework to understand the ballistic transfer trajectories, but the design of the real-world equivalent trajectories often requires a landing or launching at either higher or lower latitudes. The spatial ballistic transfer trajectories using the periodic orbits of Family 26 and their invariant manifolds are shown in Fig. 13(b) It is noted that the same definition in the planar problem is applied for α and β is measured like latitude and is positive above the xy-plane.

The landing and launching areas as illustrated in Fig. 16. The dash lines indicate the projection of the landing and launching velocities on the surface of asteroids. The color of the line indicates the elevation angle of the velocity, which varies from $-90°$ (blue) to $90°$ (orange). It can be immediately seen that the landing and launching areas present two ellipsoids in $\alpha\beta$-plane. As the energy level increases, the areas become boarder. However, when the Jacobi constant reaches a specific values (-0.3040 of Lundia), the areas become irregular and mainly group on the leading edge $\alpha = 90°$ and the trailing edge $\alpha = 270°$ for both bodies.

The landing areas with the lowest velocity of Lundia are also discussed, as shown in Table 9. It demonstrates that these areas also exist near the equator of the asteroids. Moreover, the 'velocity jump' areas are found in Fig. 16. A spacecraft on these areas will change its direction of landing or launching velocity suddenly. Probably it will lead a spacecraft be out of control when landing or launching. Thus the further mission design of ballistic transfer should take these points into consideration to ensure the success of landing and launching processes.

5 Conclusion

This paper investigates the periodic orbits in the gravitational field of the doubly synchronous binary asteroid systems. Two typical DSBAs, 809 Lundia and 3169 Ostro, are discussed prominently. According to the observational characterization, the two systems are modeled as two triaxial ellipsoids. The gravitational potential of the systems is calculated based on the Ivory's theorem. The zero-velocity curves and equilibrium points of the systems are discussed and all of the equilibrium points of the systems proved to be nonlinearly unstable. Next, systematic searches of global periodic orbits around Lundia and Ostro are conducted by a numerical method combing grid searching and differential correction. A total of 30 families of periodic orbits around Lundia and 28 families of periodic orbits around Ostro are generated. By characterizing the morphology, stabilities and invariant manifolds of these periodic orbits, the potential applications in space mission are discussed. Several quasi-circular orbit families with low instability index are found to be suitable for the observation of the DSBAs. Furthermore, some periodic orbits near equilibrium points and their invariant manifolds are proved to be able to offer the fuel-free landing and transfer trajectories for binary exploration mission.

References

Baoyin, H., McInnes, C.R.: Trajectories to and from the Lagrange points and the primary body surfaces. J. Guid. Control Dyn. **29**(4), 998–1003 (2006)

Behrend, R., et al.: Four new binary minor planets: (854) Frostia, (1089) Tama, (1313) Berna, (4492) Debussy. Astron. Astrophys. **446**, 1177–1184 (2006)

Bellerose, J., Scheeres, D.J.: Restricted full three-body problem: application to binary system 1999 KW4. J. Guid. Control Dyn. **31**(1), 162–171 (2008a)

Bellerose, J., Scheeres, D.J.: Dynamics and control for surface exploration of small bodies. In: Proceedings of AIAA/AAS 2008 Astrodynamics Specialist Conference, pp. 18–21 (2008b)

Chandrasekhar, S.: Ellipsoidal Figures of Equilibrium, p. 43. Yale University Press, New Haven (1969)

Descamps, P.: Roche figures of doubly synchronous asteroids. Planet. Space Sci. **56**(14), 1839–1846 (2008)

Descamps, P., et al.: Figure of the double Asteroid 90 Antiope from adaptive optics and lightcurve observations. Icarus **187**(2), 482–499 (2007a)

Descamps, P., et al.: Nature of the small main belt Asteroid 3169 Ostro. Icarus **189**(1), 362–369 (2007b)

Descamps, P., et al.: New determination of the size and bulk density of the binary Asteroid 22 Kalliope from observations of mutual eclipses. Icarus **196**(2), 578–600 (2008)

Dichmann, D.J., Doedel, E.J., Paffenroth, R.C.: The computation of periodic solutions of the 3-body problem using the numerical continuation software AUTO. In: Libration Point Orbits and Applications, pp. 429–488 (2003)

Gong, S.-p., et al.: Lunar landing trajectory design based on invariant manifold. Appl. Math. Mech. **28**, 201–207 (2007)

Helfenstein, P., et al.: Galileo photometry of asteroid 243 Ida. Icarus **120**(1), 48–65 (1996)

Hénon, M.: Vertical stability of periodic orbits in the restricted problem. Celest. Mech. Dyn. Astron. **8**(2), 269–272 (1973)

Herrera-Sucarrat, E., Palmer, P.L., Roberts, R.M.: Asteroid observation and landing trajectories using invariant manifolds. J. Guid. Control Dyn. **37**(3), 907–920 (2014)

Koon, W.S., et al.: Dynamical systems. the three-body problem and space mission design., 1167–1181 (2000)

Kryszczyńska, A., et al.: New binary asteroid 809 Lundia. Astron. Astrophys. **501**, 769–776 (2009)

Lo, M.W., Parker, J.S.: Unstable resonant orbits near earth and their applications in planetary missions. Paper AIAA 5304 (2004)

Margot, J.-L., et al.: Binary asteroids in the near-Earth object population. Science **296**(5572), 1445–1448 (2002)

Merline, W.J., et al.: Asteroids do have satellites. Asteroids **III**(1), 289–312 (2002)

Neutsch, W.: On the gravitational energy of ellipsoidal bodies and some related functions. Astron. Astrophys. **72**, 339–347 (1979)

Noll, K.S., et al.: Discovery of a binary Centaur. Icarus **184**(2), 611–618 (2006)

Pravec, P., Harris, A.W.: Binary asteroid population: 1. Angular momentum content. Icarus **190**(1), 250–259 (2007)

Pravec, P., et al.: Photometric survey of binary near-Earth asteroids. Icarus **181**(1), 63–93 (2006)

Russell, R.P.: Global search for planar and three-dimensional periodic orbits near Europa. J. Astronaut. Sci. **54**(2), 199–226 (2006)

Scheeres, D.J., Augenstein, S.: Spacecraft motion about binary asteroids. Adv. Astronaut. Sci. **116**, 1–20 (2004)

Scheeres, D.J., et al.: Orbits close to asteroid 4769 Castalia. Icarus **121**(1), 67–87 (1996)

Scheeres, D.J., et al.: Dynamics of orbits close to asteroid 4179 Toutatis. Icarus **132**(1), 53–79 (1998)

Tardivel, S., Scheeres, D.J.: Ballistic deployment of science packages on binary asteroids. J. Guid. Control Dyn. **36**(3), 700–709 (2013)

Tardivel, S., Michel, P., Scheeres, D.J.: Deployment of a lander on the binary asteroid (175706) 1996 FG3, potential target of the European MarcoPolo-R sample return mission. Acta Astronaut. **89**, 60–70 (2013)

Vrahatis, M.N., Iordanidis, K.I.: A rapid generalized method of bisection for solving systems of non-linear equations. Numer. Math. **49**(2–3), 123–138 (1986)

Walsh, K.J., Richardson, D.C., Michel, P.: Rotational breakup as the origin of small binary asteroids. Nature **454**(7201), 188–191 (2008)

Yu, Y.: Research on Orbital Dynamics in the Gravitational Field of Small Bodies, pp. 17–18 (2014)

Yu, Y., Baoyin, H.: Orbital dynamics in the vicinity of asteroid 216 Kleopatra. Astron. J. **143**(3), 62 (2012a)

Yu, Y., Baoyin, H.: Generating families of 3D periodic orbits about asteroids. Mon. Not. R. Astron. Soc. **427**(1), 872–881 (2012b)